Editors' Suggestion

Real-Time Observation of Charge-Spin Cooperative Dynamics Driven by a Nonequilibrium Phonon Environment

Kazuyuki Kuroyama,[1,2,3,*] Sadashige Matsuo,[1,3,4,†] Jo Muramoto,[1] Shunsuke Yabunaka,[5] Sascha R. Valentin,[6] Arne Ludwig,[6] Andreas D. Wieck,[6] Yasuhiro Tokura,[7] and Seigo Tarucha[1,3,‡]

[1]*Department of Applied Physics, The University of Tokyo, 7-3-1 Hongo, Bunkyo-ku, Tokyo 113-8656, Japan*
[2]*Institute of Industrial Science, The University of Tokyo, 4-6-1 Komaba, Meguro-ku, Tokyo 153-8505, Japan*
[3]*Center for Emergent Materials Science (CEMS), RIKEN, 2-1 Hirosawa, Wako-shi, Saitama 351-0198, Japan*
[4]*Japan Science and Technology Agency, PRESTO, 4-1-8 Honcho, Kawaguchi-shi, Saitama 332-0012, Japan*
[5]*Department of Physics, Kyushu University, Fukuoka 819-0395, Japan*
[6]*Lehrstuhl für Angewandte Festkörperphysik, Ruhr-Universität Bochum, D-44780 Bochum, Germany*
[7]*Pure and Applied Sciences, University of Tsukuba, 1-1-1 Tennodai, Tsukuba, Ibaraki 305-8571, Japan*

(Received 7 June 2021; accepted 14 July 2022; published 24 August 2022)

We report on experimental observations of charge-spin cooperative dynamics of two-electron states in a GaAs double quantum dot located in a nonequilibrium phonon environment. When the phonon energy exceeds the lowest excitation energy in the quantum dot, the spin-flip rate of a single electron strongly enhances. In addition, originated from the spatial gradient of phonon density between the dots, the parallel spin states become more probable than the antiparallel ones. These results indicate that spin is essential for further demonstrations of single-electron thermodynamic systems driven by phonons, which will greatly contribute to understanding of the fundamental physics of thermoelectric devices.

DOI: 10.1103/PhysRevLett.129.095901

A heat engine consisting of a single electron and its spin has recently attracted increased attention from the perspectives of energy harvesting and thermoelectric conversion for waste heat created in nanoscale electric devices [1,2]. In this context, a quantum dot (QD) is recognized as one of the best systems due to its high controllability of both single electron charges and their spins, and a number of related studies on QD-based heat engines have been reported to date [2–6]. In general, according to the second law of thermodynamics, to drive a thermodynamic cycle in a heat engine, a thermodynamic device must be located in the nonequilibrium environment of heat. However, in these studies, a QD heat engine is driven by electron reservoirs at different *electron* temperatures, not by thermal reservoirs at different *lattice* temperatures. This is probably because creating a lattice temperature gradient over a distance of at most a few hundred nanometers, the order of QD size, is technically challenging. A QD heat engine driven by a local lattice temperature gradient would aid understanding of thermodynamic and thermoelectric phenomena of electrons in mesoscopic systems and, regarding practical applications, for improving the coherence time of spin and charge qubits with QDs, that are sensitive to a phonon environment [7–9].

In this work, we concentrate on the real-time observation of the charge-spin cooperative dynamics of electrons in a GaAs lateral double QD (DQD) [10] in a nonequilibrium phonon environment. A QD-based phonon source that generates acoustic phonons is introduced on the one side of the DQD [11–13]. Because of the selection rule of an orbital and spin angular momentums, the intradot phonon excitation and relaxation processes of an electron needs a spin flip. Such spin-flip processes accompanied by a phonon excitation and relaxation of electrons in QDs have already been intensively discussed theoretically [14–16] and experimentally [7,17–20], but all on the static behavior. Here we first report the real-time observations of the phonon-induced spin-flip events. For the real-time observations of the phonon-induced spin-flip events, we introduce the Pauli spin-blockade (PSB) effect of a two-electron DQD [21,22] with a real-time charge sensing technique [23–25]. We use the result of the real-time experiment to investigate the statistics of the stochastic phonon-induced spin-flip events in the two-electron DQD set in the PSB regime. Our results show that the spin-flip rate increases notably when the generated phonon energy exceeds the lowest excitation energy in the DQD. Furthermore, we experimentally confirm that a phonon density gradient over the two dots is created by the phonon source and that the spin configurations in the DQD are significantly modified by the local phonon density gradient.

The gate electrode configuration of our DQD devices fabricated from a GaAs quantum well wafer is depicted in Fig. 1(a). The DQD potential is formed in the region marked in yellow by applying negative voltages on the gate electrodes TL, T, TR, L, C, and R. The Ohmic contacts are indicated by the white crosses. The charge states of the DQD are monitored by a nearby QD charge sensor located on the left side. We note that no bias voltage is applied on

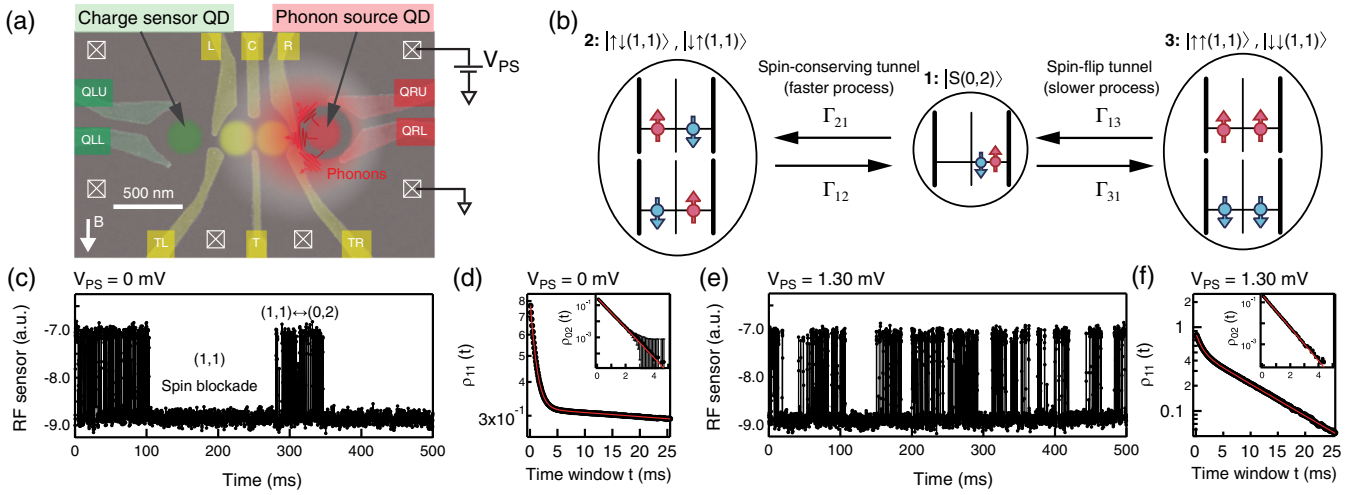

FIG. 1. (a) Scanning electron micrograph of our sample. The DQD is formed on the two yellow circles. The charge sensor is placed on the left green circle. The phonon source is located on the right red circle, on which the dc bias voltage V_{PS} is applied. (b) Transition diagram in a resonant two-electron DQD. States 1 and 2 (1 and 3) are connected by the spin-conserving (spin-flip) tunnels. (c),(e) Typical time traces of the rf charge sensing signal on the (0,2)-(1,1) resonance condition with and without phonon irradiation, respectively. (d),(f) FCS distributions regarding the (1,1) charge state, $\rho_{11}(0,t)$, at $V_{PS} = 0$ and 1.30 mV, respectively. The fitted functions are colored red. The insets are the FCS distribution of the (0,2) charge state, $\rho_{02}(0,t)$.

the charge sensor to obtain the highest sensitivity, and thus, no phonon emission from the sensor QD is expected.

To generate nonequilibrium phonons, we separately install an additional QD formed right next to the DQD as shown in red [see Fig. 1(a)] [12,13,17,26]. A relatively large dc bias voltage V_{PS} is applied on the QD, injecting hot electrons, which accompanies phonon emissions through the inelastic relaxation process. Therefore, this QD is regarded as a phonon source. We note that the highest phonon energy emitted from the source is eV_{PS} [12].

We set the gate voltages, L and R, such that the chemical potentials of the two dots are equivalent between the lowest (1,1) and (0,2) charge states, where the integers (i,j) in the bracket denote the electron occupations of the left and right dot, respectively. The lowest (0,2) state is a spin singlet $(|S(0,2)\rangle = (|\uparrow\downarrow(0,2)\rangle - |\downarrow\uparrow(0,2)\rangle)/\sqrt{2})$. For a weakly coupled DQD, the lowest spin eigenstates of the (1,1) charge state are $|\uparrow\downarrow(1,1)\rangle$ and $|\downarrow\uparrow(1,1)\rangle$ for antiparallel spins, and $|\uparrow\uparrow(1,1)\rangle$ and $|\downarrow\downarrow(1,1)\rangle$ for parallel spins [27,28].

To turn on the PSB, we apply an in-plane magnetic field of 100 mT. In the PSB regime, $|\uparrow\uparrow(1,1)\rangle$ and $|\downarrow\downarrow(1,1)\rangle$ are not able to tunnel to $|T_{\pm}(0,2)\rangle$, because $|T_{\pm}(0,2)\rangle$ are much higher energy than $|S(0,2)\rangle$. Therefore, for $|\uparrow\uparrow(1,1)\rangle$ and $|\downarrow\downarrow(1,1)\rangle$, the interdot electron tunneling to $|S(0,2)\rangle$ only occurs when accompanied by a spin flip to break the PSB. There are two possible spin-flip mechanisms for a GaAs QD: the spin-orbit interaction during the interdot charge tunnel [27,28] and the hyperfine interaction in each dot [29]. A number of previous studies have already shown that the spin-orbit interaction is more dominant in our experimental condition (see Supplemental Material, Sec. VII [30]). Therefore, we only consider the spin-orbit interaction in the following discussions, and then assume a transition diagram of the two-electron spin states as shown in Fig. 1(b). In this figure, Γ_{ij} indicates the tunnel rate in the transition from the electron state j to i. Γ_{21} and Γ_{12} are the spin-conserving tunnel rates, while Γ_{31} and Γ_{13} are the spin-flip tunnel rates. We note that the spin-flip tunneling is usually much slower than the spin-conserving tunneling.

First, we measure the interdot resonant tunneling in the PSB regime with no phonon irradiation, i.e., $V_{PS} = 0$ mV. Figure 1(c) depicts an obtained typical time trace of the rf charge sensing signal. The time trace shows a two-level telegraph signal, indicating that the DQD charge state is either (0,2) or (1,1). Between 0 and 100 ms, and between 285 and 350 ms, fast interdot transitions between the (0,2) and (1,1) charge states are observed iteratively, implying that the spin configuration is antiparallel [see Fig. 1(b)]. In contrast, the stable region, in which the charge state stays at (1,1) for a long time from 100 to 285 ms and from 350 to 500 ms, appears due to the prohibition of the charge transition by the PSB effect. Therefore, the spin configuration in this blockade region is supposed to be parallel, either $|\uparrow\uparrow(1,1)\rangle$ or $|\downarrow\downarrow(1,1)\rangle$.

We use the full counting statistics (FCS) method to evaluate the spin-conserving and spin-flip tunnel rates from the experimental data, considering a probability of n instances of interdot tunneling for a certain time window t and a final charge state of either (1,1) or (0,2) [35]. In the following discussion, we focus on only the probability of $n = 0$, which is the same as that of state (1,1) [or (0,2)] without any interdot tunneling in the time window t. In this situation, we omit the notation n for simplicity. The FCS probability distributions of the (1,1) charge state $[\equiv\rho_{11}(t)]$

and the (0,2) state [$\equiv\rho_{02}(t)$] are analytically derived as follows.

$$\rho_{11}(t) = C_2 e^{-\Gamma_{12}t} + C_3 e^{-\Gamma_{13}t}, \quad (1)$$

$$\rho_{02}(t) = C_1 e^{-(\Gamma_{21}+\Gamma_{31})t}, \quad (2)$$

where the coefficient of C_i ($i = 1, 2, 3$) is the occupation probability at state i depicted in Fig. 1(b). These coefficients are represented by the ratios of the transition rates as explained in Supplemental Material, Sec. VI [30]. Figure 1(d) depicts the probability distributions $\rho_{11}(t)$ [inset: $\rho_{02}(t)$] constructed from the measured time traces. For the $\rho_{11}(t)$, we clearly observe a steep and loose slope. These two slopes are assigned to the spin-conserving (Γ_{12}) and spin-flip (Γ_{13}) tunnel processes, corresponding to the $e^{-\Gamma_{12}t}$ and $e^{-\Gamma_{13}t}$ terms in Eq. (1), respectively. The red curve is the fitted function of Eq. (1) [inset: Eq. (2)] to the experimental data. From this fitting and using our compensation technique discussed in Supplemental Material, Sec. V [30], Γ_{12} of 1.21 kHz and Γ_{13} of 3.51 Hz are obtained. The remaining transition rates of $\Gamma_{21} = 2.32$ kHz and $\Gamma_{31} = 4.80$ Hz are evaluated as well, using the coefficients and exponent of $\rho_{02}(t)$.

Subsequently, we turn on the phonon source by applying a finite bias voltage V_{PS}. Figure 1(e) is a typical time trace measured for $V_{\mathrm{PS}} = 1.30$ mV. Compared to the result at $V_{\mathrm{PS}} = 0$ mV in Fig. 1(c), the blockade times at the (1,1) state are shorter. This shorter blockade time can be interpreted as the spin-flip tunnel processes occurring more frequently under phonon irradiation. For quantitative comparison, the FCS probability distributions measured at $V_{\mathrm{PS}} = 1.30$ mV are indicated in Fig. 1(f). We again see a definite feature of a double-exponential function in the $\rho_{11}(t)$ distribution, but only the second slope reflecting the spin-flip tunnel rate becomes steeper as a larger bias voltage is applied. Using the same analysis as for Fig. 1(c), Γ_{12} of 1.06 kHz, Γ_{21} of 1.70 kHz, Γ_{13} of 88.9 Hz, and Γ_{31} of 170 Hz are obtained. Thus, we confirm that the spin-flip tunnel rates Γ_{13}, Γ_{31} increase more than tenfold by phonon irradiation.

To reveal the dependence of the transition rates on the phonon energy, we evaluate Γ_{21} and Γ_{13} at various values of V_{PS} ranging from 0 to 1.60 mV. The obtained Γ_{21} and Γ_{13} are plotted by the blue and red closed circles in Fig. 2(a), respectively. Both Γ_{21} and Γ_{13} are unchanged for $V_{\mathrm{PS}} < 0.90$ mV, but for further increasing V_{PS}, Γ_{13} significantly increases, whereas Γ_{21} gradually decreases. As the spin-orbit effect is determined by the material and the relative orientation of the QD array to the crystallographic axis and the magnetic field direction (see Supplemental Material, Secs. II and VII) [14,30,36], the ratio of Γ_{13}/Γ_{21} is anticipated to be constant. Therefore, the obtained enhancement of Γ_{13} cannot be explained by the spin-orbit effect of the ground states. Moreover, phonons have only a little effect

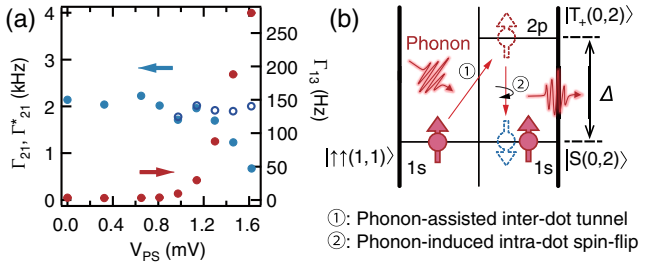

FIG. 2. (a) Spin-conserving tunnel rate Γ_{21} (filled blue circles) and spin-flip tunnel rate Γ_{13} (red circles) with respect to V_{PS}. We additionally plot Γ^*_{21} evaluated by the five-state FCS calculation with open deep-blue circles (see Supplemental Material, Sec. VI [30]). (b) Energy level diagram in a DQD, which explains the phonon-induced spin-flip tunneling process, $|\uparrow\uparrow(1,1)\rangle \rightarrow |T_+(0,2)\rangle \rightarrow |S(0,2)\rangle$.

on the interdot transitions between the ground states as discussed in Supplemental Material, Sec. IV [30].

Since the enhancement of the spin-flip tunnel rate is observed only when the phonon energy exceeds the threshold voltage of approximately $V_{\mathrm{PS}} \sim 0.90$ mV, it is reasonable to assume that the excitation processes in the DQD play an important role. To explain the observed spin-flip rate enhancements, we propose its mechanism based on previous theoretical work [15] and on the alignment of two-electron spin states as shown in Fig. 2(b). The increase in the spin-flip tunnel rates is explained by a combination of "the phonon-assisted interdot transition with spin conservation between $|T_+(0,2)\rangle$ ($|T_-(0,2)\rangle$) and $|\uparrow\uparrow(1,1)\rangle$ ($|\downarrow\downarrow(1,1)\rangle$)" and "the intradot spin-flip transition between $|T_\pm(0,2)\rangle$ and $|S(0,2)\rangle$." Here, we explain the transition process starting from the (1,1) charge state with parallel spins subject to the PSB. As the interdot coupling is sufficiently weak, an electron in each dot is located mainly in the s-type orbital. When phonon energy compensates the energy separation between $|T_\pm(0,2)\rangle$ and $|T_0(0,2)\rangle$, Δ (see Supplemental Material, Sec. III for Δ estimation [30]), an interdot transition from $|\uparrow\uparrow(1,1)\rangle$ ($|\downarrow\downarrow(1,1)\rangle$) to $|T_+(0,2)\rangle$ ($|T_-(0,2)\rangle$) is allowed. Although one of the electrons is excited between the orbitals with different angular momentum, i.e., from the s-type orbital to the p-type orbital, this interdot transition is still allowed because of the lack of rotational symmetry of the DQD. Subsequently, $|T_\pm(0,2)\rangle$ swiftly relaxes to $|S(0,2)\rangle$ by the simultaneous action of the spin-orbit interaction and the electron-phonon interaction, because the spin-orbit interaction hybridizes the singlet and triplet states of the (0,2) charge state [15]. This spin-flip relaxation process takes place within a few hundred microseconds [18,19,37], much faster than the other transitions, because of the larger dipole moment of the p-type orbital wave function [15].

From the above discussion, we assign the first excited states of $|T_\pm(0,2)\rangle$ as responsible for the enhancement of the spin-flip tunnel rates. Therefore, we exploit our

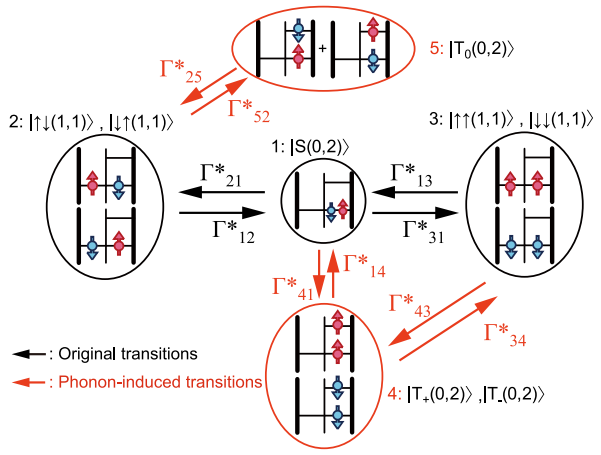

FIG. 3. Transition diagram used for the five-state FCS calculation. The newly added transitions are depicted by red arrows, and are induced by phonon irradiation. The transitions between states 3 and 4 and between 2 and 5 are phonon-assisted interdot tunneling without a spin flip, whereas those between states 1 and 4 are the phonon-induced spin-flip processes occurring in the right dot.

model by differentiating the (0,2) charge state into the ground state ($|S(0,2)\rangle$) and the three excited states ($|T_{\pm}(0,2)\rangle, |T_0(0,2)\rangle$). The transition diagram is modified as depicted in Fig. 3. Both the spin-flip intradot and spin-conserving interdot transitions are mediated by a phonon process. Here, the transition rate Γ^*_{ij} from state j to i is newly defined as the value evaluated using FCS for five states (Fig. 3), to avoid confusion with the rates Γ_{ij} evaluated used FCS for three states [Fig. 1(b)]. The excited state 4 ($|T_{\pm}(0,2)\rangle$) is accessed from state 3 with the phonon-assisted, spin-conserving interdot tunneling and also from state 1 with the intradot spin-flip process. It should be noted that the phonon-assisted interdot transitions between $|T_0(0,2)\rangle$ and $|\uparrow\downarrow(1,1)\rangle$ (or $|\uparrow\downarrow(1,1)\rangle$) are also available. However, the transition between $|T_0(0,2)\rangle$ and $|S(0,2)\rangle$ may be very slow because of the selection rule of the total angular momentum conservation in the spin-orbit interaction [7,19]. Therefore, we dismiss this transition in the FCS computation. We derive a set of FCS differential equations (see Supplemental Material, Sec. VI [30]) and obtain the following FCS distributions for the (1,1) and (0,2) charge states.

$$\rho^*_{11}(t) = C_2 e^{-(\Gamma^*_{12}+\Gamma^*_{52})t} + C_3 e^{-(\Gamma^*_{13}+\Gamma^*_{43})t}, \tag{3}$$

$$\rho^*_{02}(t) = (C^*_1 + C^*_4)e^{-\lambda^*_- t} + C^*_5 e^{-\Gamma^*_{25} t}. \tag{4}$$

The coefficient of C^*_i ($i = 1, 4, 5$) is the occupation probability of state i, which is one of the (0,2) charge states, and the relation $C^*_1 + C^*_4 + C^*_5 = C_1$ is satisfied. λ^*_- is no longer expressed in a simple manner like $\rho_{02}(t)$ in Eq. (2). We explain how to derive λ^*_- in Supplemental Material, Sec. VI [30]. Similar to the three-state FCS, the distribution $\rho^*_{11}(t)$ consists of a double exponential function, and it clearly shows that the increase in the second slope of $\rho^*_{11}(t)$ originates from the phonon-assisted interdot tunnel rate Γ^*_{43}, whereas Γ^*_{13} (and Γ^*_{31}) may be much less affected by phonons. For $\rho^*_{02}(t)$, the measured distribution resembles the single exponential function [inset of Fig. 1(f)] for all $V_{\rm PS}$, however, the calculation predicts a double exponential function. Therefore, to achieve the consistency with the measured distribution, at least one of the following conditions must be satisfied: "*occupation probability of state 5, C^*_5 is much smaller than $C^*_1 + C^*_4$*" and "Γ^*_{25} *takes a similar value to λ^*_- (~ 2 kHz)*". In fact, we confirmed that both of them hold for our experimental conditions and that the former is the most important.

Using the five-state FCS, we discuss the nonequilibrium properties of the phonon-induced charge-spin dynamics. Because the distances from the phonon source to the left and right QDs are different, the phonon density is different at the two dot positions if the generated phonon is in nonequilibrium. Indeed, we can estimate the effective phonon temperature for the right QD by assuming the Boltzmann distribution $\Gamma^*_{41}/(2\Gamma^*_{14}) = \exp[-\Delta/(k_B T_{\rm ph\_14})]$, for the phonon-induced transitions, Γ^*_{14} and Γ^*_{41}. Similarly, the effective phonon temperature can be defined for phonon-induced interdot tunneling between state 3 and 4 as $\Gamma^*_{43}/\Gamma^*_{34} = \exp[-\Delta/(k_B T_{\rm ph\_34})]$. These ratios of the transition rates can be evaluated using the five-state FCS (see Supplemental Material, Sec. VIII [30]). Thus, the calculated effective phonon temperatures $T_{\rm ph\_34}$ and $T_{\rm ph\_14}$ are plotted in Fig. 4(a) as a function of $V_{\rm PS}$. As expected, the latter temperature at the right QD increases more significantly. This indicates the phonon density gradient created between the two dots of the DQD. This effective temperature gradient induces an imbalance in the occupation probabilities of the electron spins in the (1,1) charge state. Figure 4(b) shows the occupation probabilities of the (0,2) charge state ($C^*_1 + C^*_4 + C^*_5$) and states 2 and 3 of the (1,1) charge state in regard to $V_{\rm PS}$. At lower $V_{\rm PS}$, these occupation probabilities are approximately 0.2, 0.4, and 0.4, respectively. In this case, as the spin state is mostly one of states 1, 2, and 3, these probabilities are determined by the number of available internal states in states 1, 2, and 3. For higher $V_{\rm PS}$, however, the occupation probability of state 3 increases from 0.4, whereas that of state 2 decreases. In contrast, the occupation probability of the (0,2) charge state remains at 0.2. This indicates that the occupation probability of the (1,1) charge state is transferred from state 2 to 3, and the parallel spin configuration becomes more probable. This can be understood by the imbalance of the spin-flip tunnel rates, which is discussed in Supplemental Material, Sec. VIII [30].

In conclusion, we study the charge-spin cooperative dynamics in a DQD under a nonequilibrium phonon environment. The spin-flip tunnel rates are significantly

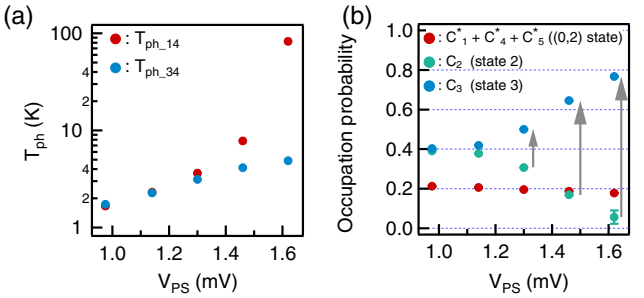

FIG. 4. (a) Effective phonon temperatures plotted as a function of V_{PS}. (b) Occupation probabilities of the (0,2) charge state and states 2 and 3 depicted in Fig. 3. For states 2 and 3 of the (1,1) charge state, the occupation probability of parallel spin configurations (C_3) increases, whereas that of antiparallel spin configurations (C_2) decreases.

enhanced when the maximum energy of the generated acoustic phonons exceeds the lowest excitation energy in the QD, explained by the spin-flip process intermediated by $|T_{\pm}(0,2)\rangle$ with phonon excitation. Finally, we confirmed the spatial gradient of the phonon density between the two dots, indicating the local temperature gradient over the DQD. The occupation probabilities of the spin states are strongly modified by the nonequilibrium phonon distribution when the phonon density gradient increases. Our findings may promote new concepts of spin-dependent DQD heat engines and thermoelectric devices that are driven by a local lattice temperature gradient.

This work was supported by a the Grant-in-Aid for Scientific Research (S) (No. JP19H05610), JST CREST (No. JPMJCR15N2), JST PRESTO (No. JPMJPR18L8), JSPS Research Fellowship for Young Scientists (No. JP16J03037, No. JP19J01737) and RIKEN-Kyudai Science and Technology Hub Collaborative Research Program. A. D. W., A. L., and S. R. V gratefully acknowledge the support of DFG-TRR160, BMBF-Q.com-H 16KIS0109, and the DHF/UFA CDFA-05-06. Y. T. is supported by a Grant-in-Aid for Scientific Research (C) (No. JP18K03479).

*kuroyama@iis.u-tokyo.ac.jp
†sadashige.matsuo@riken.jp
‡tarucha@riken.jp

[1] B. Roche, P. Roulleau, T. Jullien, Y. Jompol, I. Farrer, D. A. Ritchie, and D. C. Glattli, Nat. Commun. **6**, 6738 (2015).
[2] G. Jaliel, R. K. Puddy, R. Sánchez, A. N. Jordan, B. Sothmann, I. Farrer, J. P. Griffiths, D. A. Ritchie, and C. G. Smith, Phys. Rev. Lett. **123**, 117701 (2019).
[3] H. Thierschmann, R. Sánchez, B. Sothmann, F. Arnold, C. Heyn, W. Hansen, H. Buhmann, and L. W. Molenkamp, Nat. Nanotechnol. **10**, 854 (2015).
[4] M. Josefsson, A. Svilans, A. M. Burke, E. A. Hoffmann, S. Fahlvik, C. Thelander, M. Leijnse, and H. Linke, Nat. Nanotechnol. **13**, 920 (2018).
[5] K. Ono, S. N. Shevchenko, T. Mori, S. Moriyama, and F. Nori, Phys. Rev. Lett. **125**, 166802 (2020).
[6] M. Josefsson, A. Svilans, H. Linke, and M. Leijnse, Phys. Rev. B **99**, 235432 (2019).
[7] T. Meunier, I. T. Vink, L. H. Willems van Beveren, K.-J. Tielrooij, R. Hanson, F. H. L. Koppens, H. P. Tranitz, W. Wegscheider, L. P. Kouwenhoven, and L. M. K. Vandersypen, Phys. Rev. Lett. **98**, 126601 (2007).
[8] V. Kornich, C. Kloeffel, and D. Loss, Phys. Rev. B **89**, 085410 (2014).
[9] A. Purkayastha, G. Guarnieri, M. T. Mitchison, R. Filip, and J. Goold, Quantum Inf. **6**, 27 (2020).
[10] R. Hanson, L. P. Kouwenhoven, J. R. Petta, S. Tarucha, and L. M. K. Vandersypen, Rev. Mod. Phys. **79**, 1217 (2007).
[11] D. Taubert, M. Pioro-Ladrière, D. Schröer, D. Harbusch, A. S. Sachrajda, and S. Ludwig, Phys. Rev. Lett. **100**, 176805 (2008).
[12] D. Harbusch, D. Taubert, H. P. Tranitz, W. Wegscheider, and S. Ludwig, Phys. Rev. Lett. **104**, 196801 (2010).
[13] G. Granger, D. Taubert, C. E. Young, L. Gaudreau, A. Kam, S. A. Studenikin, P. Zawadzki, D. Harbusch, D. Schuh, W. Wegscheider, Z. R. Wasilewski, A. A. Clerk, S. Ludwig, and A. S. Sachrajda, Nat. Phys. **8**, 522 (2012).
[14] J. Danon, Phys. Rev. B **88**, 075306 (2013).
[15] V. N. Golovach, A. Khaetskii, and D. Loss, Phys. Rev. B **77**, 045328 (2008).
[16] V. N. Golovach, A. Khaetskii, and D. Loss, Phys. Rev. Lett. **93**, 016601 (2004).
[17] G. Cao, M. Xiao, H. Li, C. Zhou, R. Shang, T. Tu, H. Jiang, and G. Guo, New J. Phys. **15**, 023021 (2013).
[18] T. Fujisawa, D. G. Austing, Y. Tokura, Y. Hirayama, and S. Tarucha, Nature (London) **419**, 278 (2002).
[19] S. Sasaki, T. Fujisawa, T. Hayashi, and Y. Hirayama, Phys. Rev. Lett. **95**, 056803 (2005).
[20] R. Hanson, L. H. W. van Beveren, I. T. Vink, J. M. Elzerman, W. J. M. Naber, F. H. L. Koppens, L. P. Kouwenhoven, and L. M. K. Vandersypen, Phys. Rev. Lett. **94**, 196802 (2005).
[21] K. Ono, D. G. Austing, Y. Tokura, and S. Tarucha, Science **297**, 1313 (2002).
[22] A. C. Johnson, J. R. Petta, C. M. Marcus, M. P. Hanson, and A. C. Gossard, Phys. Rev. B **72**, 165308 (2005).
[23] W. Lu, Z. Ji, L. Pfeiffer, K. W. West, and A. J. Rimberg, Nature (London) **423**, 422 (2003).
[24] L. M. K. Vandersypen, J. M. Elzerman, R. N. Schouten, L. H. Willems van Beveren, R. Hanson, and L. P. Kouwenhoven, Appl. Phys. Lett. **85**, 4394 (2004).
[25] R. Schleser, E. Ruh, T. Ihn, K. Ensslin, D. C. Driscoll, and A. C. Gossard, Appl. Phys. Lett. **85**, 2005 (2004).
[26] U. Gasser, S. Gustavsson, B. Küng, K. Ensslin, T. Ihn, D. C. Driscoll, and A. C. Gossard, Phys. Rev. B **79**, 035303 (2009).
[27] V. F. Maisi, A. Hofmann, M. Röösli, J. Basset, C. Reichl, W. Wegscheider, T. Ihn, and K. Ensslin, Phys. Rev. Lett. **116**, 136803 (2016).
[28] T. Fujita, P. Stano, G. Allison, K. Morimoto, Y. Sato, M. Larsson, J.-H. Park, A. Ludwig, A. D. Wieck, A. Oiwa, and S. Tarucha, Phys. Rev. Lett. **117**, 206802 (2016).

[29] A. V. Khaetskii, D. Loss, and L. Glazman, Phys. Rev. Lett. **88**, 186802 (2002).

[30] See Supplemental Material at http://link.aps.org/supplemental/10.1103/PhysRevLett.129.095901 for the wafer profile and the basics of the experiment setup (Sec. I), discussions about the possible spin-flip mechanisms (Sec. II), the evaluation of the lowest excitation energy of the DQD (Sec. III), discussions of the electron temperature under phonon irradiation (Sec. IV), the correction of our FCS method for missed interdot tunneling events (Sec. V), the derivation of the FCS distributions of two-electron spin states (Sec. VI), and the imbalance of the spin-flip tunnel rates under phonon irradiation (Sec. VII), which includes Refs. [31–34].

[31] A. Hofmann, V. F. Maisi, T. Krähenmann, C. Reichl, W. Wegscheider, K. Ensslin, and T. Ihn, Phys. Rev. Lett. **119**, 176807 (2017).

[32] D. Imanaka, S. Sharmin, M. Hashisaka, K. Muraki, and T. Fujisawa, Phys. Rev. Lett. **115**, 176802 (2015).

[33] R. Hanson, L. M. K. Vandersypen, L. H. Willems van Beveren, J. M. Elzerman, I. T. Vink, and L. P. Kouwenhoven, Phys. Rev. B **70**, 241304 (2004).

[34] A. Hofmann, C. Karlewski, A. Heimes, C. Reichl, W. Wegscheider, G. Schön, K. Ensslin, T. Ihn, and V. F. Maisi, Phys. Rev. Research **2**, 033230 (2020).

[35] S. Matsuo, K. Kuroyama, S. Yabunaka, S. R. Valentin, A. Ludwig, A. D. Wieck, and S. Tarucha, Phys. Rev. Research **2**, 033120 (2020).

[36] A. Hofmann, V. F. Maisi, T. Krähenmann, C. Reichl, W. Wegscheider, K. Ensslin, and T. Ihn, Phys. Rev. Lett. **119**, 176807 (2017).

[37] R. Hanson, L. H. W. van Beveren, I. T. Vink, J. M. Elzerman, W. J. M. Naber, F. H. L. Koppens, L. P. Kouwenhoven, and L. M. K. Vandersypen, Phys. Rev. Lett. **94**, 196802 (2005).